ACS OMEGA

http://pubs.acs.org/journal/acsodf

Article

Evaluating the Role of Molecular Heredity in the Optical and Electronic Properties of Cross-Conjugated Benzo[1,2-*d*:4,5-*d*′]bisoxazoles

David L. Wheeler, Alex V. Diodati, Aimée L. Tomlinson, and Malika Jeffries-EL*

Cite This: *ACS Omega* 2020, 5, 12374−12384

Read Online

ACCESS | Metrics & More | Article Recommendations | Supporting Information

ABSTRACT: A series of eight benzo[1,2-*d*:4,5-*d*′]bisoxazole (BBOs) were synthesized using the heredity principle as a design motif, whereby we investigated which characteristics of the linear parents were inherited by their cross-conjugated children. Four linear parents bearing 4-*tert*-butylbenzene (**P**) or 1,3-bis(4-*tert*-butylphenyl)benzene (**M**) at either the 2,6- or 4,8-position on the BBO and four cross-conjugated children bearing various combinations of the two isoelectronic aryl substituents were evaluated. Due to the bulky nature of the **M** substituent compared to that of the **P** substituent, the influence of steric hindrance along the BBO axes was explored theoretically and experimentally. The optical and electronic properties of each molecule were investigated in the solution and solid state using density functional theory (DFT) and time-dependent DFT (TD-DFT) and characterized using ultraviolet photoelectron spectroscopy (UPS), ultraviolet−visible (UV−vis) spectroscopy, and photoluminescence (PL) spectroscopy. The well-correlated theoretical and experimental results showed that the selective tuning of the highest occupied molecular orbital (HOMO) and lowest unoccupied molecular orbital (LUMO) energy levels was possible through the strategic placement of substituents without impacting the H → L transition energy. Specifically, the theoretical results demonstrated that for the BBO children the HOMO and LUMO energy levels were inherited from the 4,8- and 2,6-parents, respectively. Each molecule was found to exhibit emission maxima ≤451 nm, making them ideal candidates for blue organic light-emitting diode (OLED) materials.

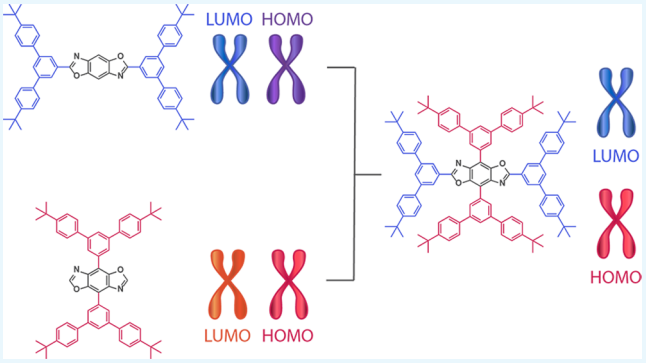

INTRODUCTION

In recent years, there has been increased interest in the development of organic semiconductors (OSCs) due to the impact these materials can have on a myriad of technologies.[1−3] Two attractive features of these materials are the opportunity to fabricate devices using solution processing and the ability to fine-tune their optical and electronic properties via chemical synthesis. As a result, it is possible to produce materials with tailored properties for specific applications.[4,5] In theory, it should be possible to attain any combination of energy levels and optical band gaps (E_g^{opt}). Experimentally, this is often challenging as the optical and electronic properties of organic semiconductors are dependent on their structures but significantly influenced by the conformations and morphologies they adapt.

Recently, a new design motif for tuning the optoelectronic properties of organic semiconductors called the "heredity principle" has been introduced.[6,7] This term, co-opted from biology, indicates that the characteristics of progeny are acquired from their parents. In terms of molecular design, it is a combinatorial approach in which two distinct moieties, or "parents", that exhibit specific optoelectronic traits are combined using an electronically orthogonal linker. As a result, the individual traits of the parents can be independently and simultaneously expressed. The molecular hybrid that results from this union is referred to as the "child" and possess unique properties that are a combination of its inherited traits. Using this approach, a single molecule exhibiting white-light emission was attained from a child that inherited both the blue and yellow emission of its parents.[6,7]

Our group has been interested in developing materials based on the benzo[1,2-*d*:4,5-*d*′]bis(oxazole) (BBO) moiety because the orthogonal arrangement of the conjugation pathways creates spatially segregated frontier molecular orbitals (FMOs).[8−14] As a result, the highest occupied molecular orbitals (HOMOs) of these materials can be nearly autonomously tuned from their lowest unoccupied molecular

Received: March 13, 2020
Accepted: May 8, 2020
Published: May 21, 2020

https://dx.doi.org/10.1021/acsomega.0c01126
ACS Omega 2020, 5, 12374−12384

orbitals (LUMOs) by changing the substituents along the 4,8-axis. However, the LUMO level can be modified by varying the substituents along the 2,6-axis with minimal impact on the HOMO level (Figure 1).[9]

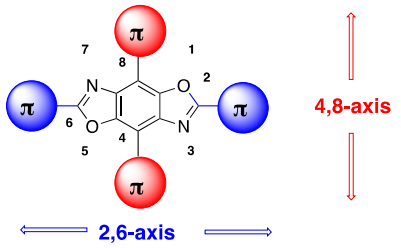

Figure 1. Conjugation pathways of the benzo[1,2-*d*:4,5-*d*′]bis(oxazole) moiety and positional assignments.

While our previous results have provided insights into the interplay between structure and optoelectronic properties in these systems, the role of steric effects has yet to be examined. In this work, we evaluate these effects by investigating two isoelectronic aryl groups; 4-*tert*-butylbenzene (**P**) and 1,3-bis(4-*tert*-butylphenyl)benzene (**M**). The *tert*-butyl substituent on the **P** group provides solubility, while its placement away from the BBO core minimizes steric hindrance. The *meta*-conjugation of additional phenyl substituents on the **M** group increases steric bulk, without increasing the conjugation length. Eight molecules were synthesized by incorporating these two aryl moieties on the BBO group. The four parent molecules have substituents along either the 2,6- or 4,8-axis of the BBO, while the four offspring are cross-conjugated molecules, or cruciforms, bearing substituents along both axes. The detailed structure−property relationships were investigated within these systems, and the influence of steric hindrance was elucidated.

RESULTS AND DISCUSSION

Synthesis and Characterization. The synthetic pathways used to achieve the phenyl precursor molecules are illustrated in Scheme 1. The synthesis of both the alkylated benzaldehyde

Scheme 1. Synthesis of Functional Phenyl Substituents[a]

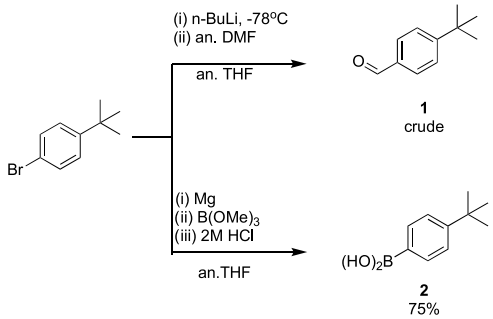

[a]Roman numerals indicate the stepwise addition of each reagent.

1 and phenylboronic acid **2** start from 4-*tert*-butylbromobenzene. This halide was either lithiated and quenched with anhydrous dimethylformamide (DMF) to create **1** or reacted with magnesium turnings to form the corresponding Grignard reagent, which was then quenched with trimethylborate and acidified to form **2**.

The synthesis of the alkylated *m*-terphenyl derivatives is shown in Scheme 2. The lithiation of tribromobenzene and its subsequent quenching with stoichiometric amounts of anhydrous DMF produced 3,5-dibromobenzaldehyde **3**, which was then subjected to Suzuki−Miyaura cross-coupling conditions with **2** to provide aldehyde **4**. However, the lithiation of tribromobenzene and its subsequent quenching with trimethylsilyl (TMS) chloride provided (3,5-dibromophenyl)trimethylsilane **5**. This product was then taken through analogous Suzuki−Miyaura cross-coupling conditions to provide the TMS-protected *m*-terphenyl derivative **6**. This product was treated with boron tribromide and potassium hydroxide to afford boronic acid **7**.

Once all precursor benzaldehydes and boronic acids were prepared, the next step was to synthesize the aryl-substituted BBOs. There are several examples in the literature where 2,6-diarylBBOs have been synthesized via condensation chemistry with aryl carboxylic acids,[15] acid chlorides,[11] or orthoesters.[16,17] While these processes form products in good yields, they require harsh reaction conditions or are hard to synthesize reagents. Therefore, we sought to find an alternative approach for their synthesis. The aryl aldehydes **1** and **2** were treated with diaminobenzoquinone and the proton-transfer catalyst, piperidine, to produce di-aryl imines that were subjected to 30% hydrogen peroxide without isolation to produce **26M** and **26P**, Scheme 3. Both **26P** and **26M** were readily recrystallized from chloroform and tetrahydrofuran, respectively. Unfortunately, using $CuSO_4$ as the catalyst to form **26P** and **26M** proved to be unsuccessful. While the yields are less than ideal, suitable quantities of material were obtained to facilitate their characterization.

The conjugation along the 4,8-axis was accomplished using Suzuki−Miyaura cross-coupling due to the low toxicity and high air-stability of the starting boronic acids, Scheme 4. Compared to traditional methods, we found that high-pressure Suzuki cross-coupling conditions using cesium fluoride as the base and a single solvent was the most efficient for our system. These conditions were employed using our aryl boronic acids and 2,6-diethyl-4,8-dibromobenzobisoxazole **8** to produce **48P** and **48M**, respectively, in good yields.

The four BBO cruciforms were made using a two-step sequence: condensation to install the aryl groups at the 2,6-position followed by Suzuki cross-coupling reactions to place aryl groups along the 4,8-axis. The condensation of 2,5-diamino-3,6-dibromobenzene-1,4-diol **8** and aldehydes **1** and **4** using $CuSO_4$ as the Lewis acid catalyst afforded the dibromo-BBOs, **26M48Br** and **26P48Br**, respectively. The subsequent cross-coupling reactions starting using **26M48Br** or **26P48Br** as the aryl halides and **2** or **7** as the boronic acids yielded **26P48P**, **26P48M**, **26M48P**, and **26M48M** in moderate to low yields, Scheme 5. All final molecules required no workup and were directly concentrated onto silica gel and purified via column chromatography. All eight compounds were low to moderately soluble in chloroform and characterized by NMR and high-resolution mass spectroscopy.

Electronic Properties. The experimentally determined values for the HOMO and optical H → L transition energies (E_g^{opt}) along with the density functional theory (DFT)-predicted values for the HOMO, LUMO, and E_g^{opt} are listed in Table 1. Due to the inaccuracies associated with DFT-predicted LUMO energies, a detailed comparison of experimental values is not discussed. Since many of the BBOs did not exhibit a redox cycle within the solvent window

https://dx.doi.org/10.1021/acsomega.0c01126
ACS Omega 2020, 5, 12374−12384

Scheme 2. Synthesis of Functional *m*-Phenyl Substituents[a]

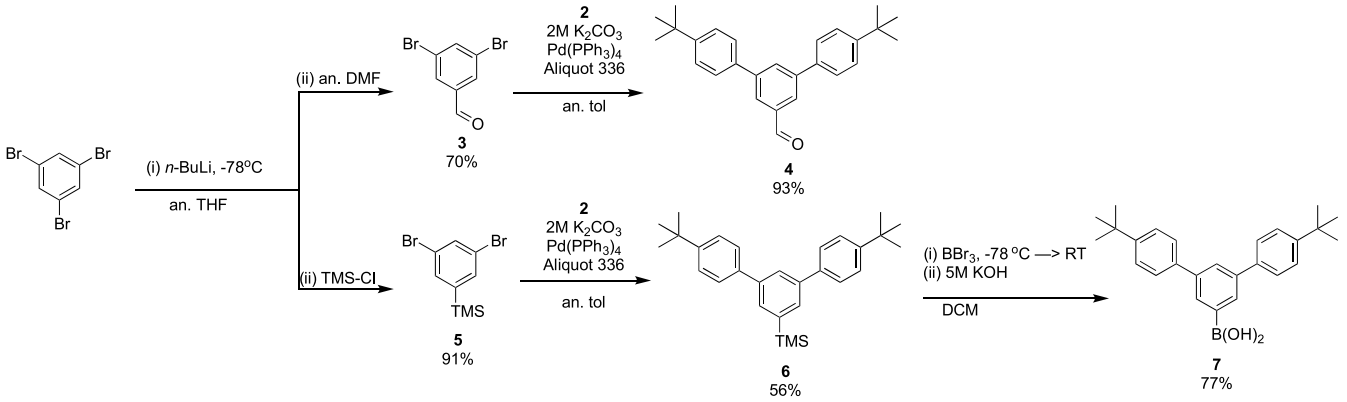

[a]Roman numerals indicate the stepwise addition of each reagent.

Scheme 3. Synthesis of 2,6-Aryl-Substituted BBOs[a]

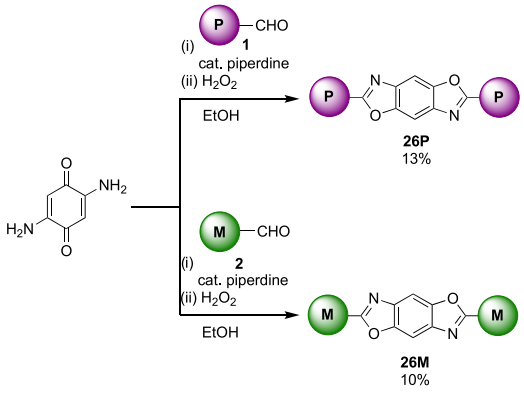

[a]Roman numerals indicate the stepwise addition of each reagent.

for the solvent/counterion blend used, we elected to use ultraviolet photoelectron spectroscopy (UPS) instead of electrochemistry to determine the HOMO levels. This technique is also beneficial as it provides an absolute determination of the HOMO level.[18−20]

Overall, there was a good correlation between theoretical and experimental HOMO results for the BBO parents **26P**, **26M**, **48P**, and **48M**. In most cases, the difference between experimental and theoretical results was less than 0.2 eV with the exception of **26P**. Based on the theoretical results, the 2,6-substituted BBOs **26P** and **26M** have deeper HOMOs than the 4,8-substituted BBOs **48P** and **48M**, respectively. However, the experimental results indicate that **26P** has the highest HOMO of all of the parents. This deviation is a result of the increased $\pi-\pi$ stacking and crystallinity of this molecule, which results in poor film formation and heterogeneous film morphology, both of which can negatively impact the UPS measurement. Previously, we observed a HOMO level of −5.75 eV for 2,6-bis(4-dodecylphenyl)benzo[1,2-*d*;3,4-*d*′]-bisoxazole, which only differs from **26P** in the alkyl chain length and more closely matches the theoretical value.[9] The longer side chain produced a more homogenous film morphology, resulting in more reliable UPS data.

The dihedral angle between the BBO moiety and the aryl substituents is an indication of planarity within these systems.[10] Both **26P** (180°) and **26M** (179.1°) are nearly planar, indicating that the steric effect of *m*-terphenyl

Scheme 4. Synthesis of 4,8-Diaryl-Substituted BBOs

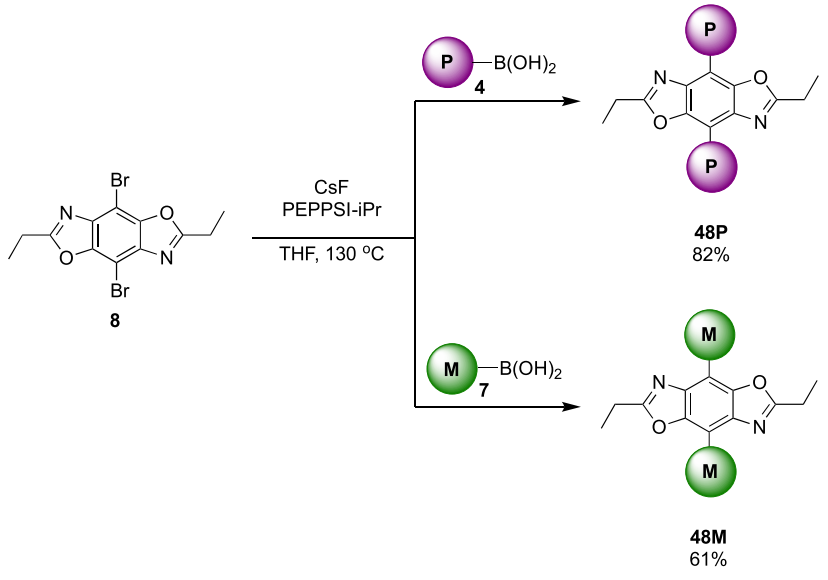

https://dx.doi.org/10.1021/acsomega.0c01126
ACS Omega 2020, 5, 12374−12384

Scheme 5. Synthesis of Cross-Conjugated BBOs[a]

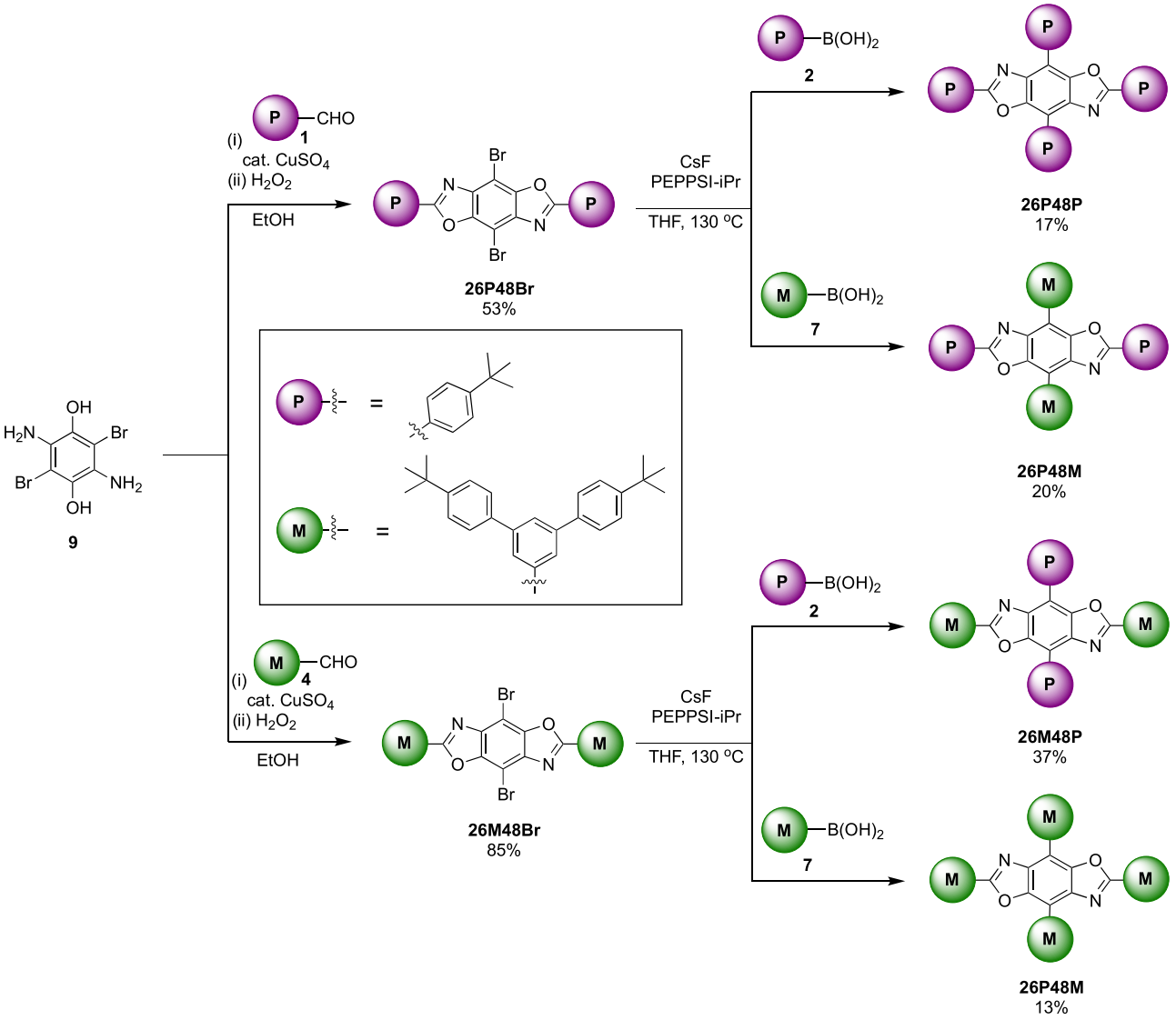

[a]Roman numerals indicate the stepwise addition of each reagent.

Table 1. Experimental (Solid-State) and Theoretical (Gas-Phase) Electronic and Geometric Properties of BBOs

	HOMO[a] (eV)		LUMO (eV)		E_g^{opt}[b] (eV)		dihedral angle (°) by axis	
BBO	exp't	DFT	exp't	DFT	exp't	DFT	4,8	2,6
26M	−6.15	−6.15	−3.05	−2.27	3.1	3.54		179.2
26P	−5.47	−6.10	−2.57	−2.20	2.9	3.60		180.0
48P	−5.73	−5.68	−2.40	−1.99	3.3	3.44	174.2	
48M	−5.95	−5.87	−2.75	−2.04	3.2	3.52	156.8	
26M48P	−5.50	−5.70	−2.50	−2.33	3.0	3.05	155.0	178.3
26P48P	−5.48	−5.66	−2.58	−2.28	2.9	3.08	155.9	176.1
26P48M	−5.62	−5.82	−2.72	−2.33	2.9	3.17	146.4	175.0
26M48M	−5.92	−5.83	−3.02	−2.33	2.9	3.17	147.0	177.6

[a]Obtained using UPS. [b]Obtained using the onset of absorbance.

substituents is negligible along the 2,6-axis. However, the steric effects are significant when the aryl groups are placed along the 4,8-axis as **48M** (157.1°) is significantly less planar than **48P** (174.2°).

Similarly, there was a good correlation between the theoretical and experimental HOMO results for the BBO children **26M48P**, **26P48P**, **26P48M**, and **26M48M**, with variances of less than 0.2 eV. We hypothesized that the cross-conjugated BBO children would inherit their HOMO energy from the 4,8-parents and their LUMO energy from the 2,6-parents. An analysis of family groupings supports this supposition, as illustrated in Figure 2. Cruciform **26M48P**

https://dx.doi.org/10.1021/acsomega.0c01126
ACS Omega 2020, 5, 12374−12384

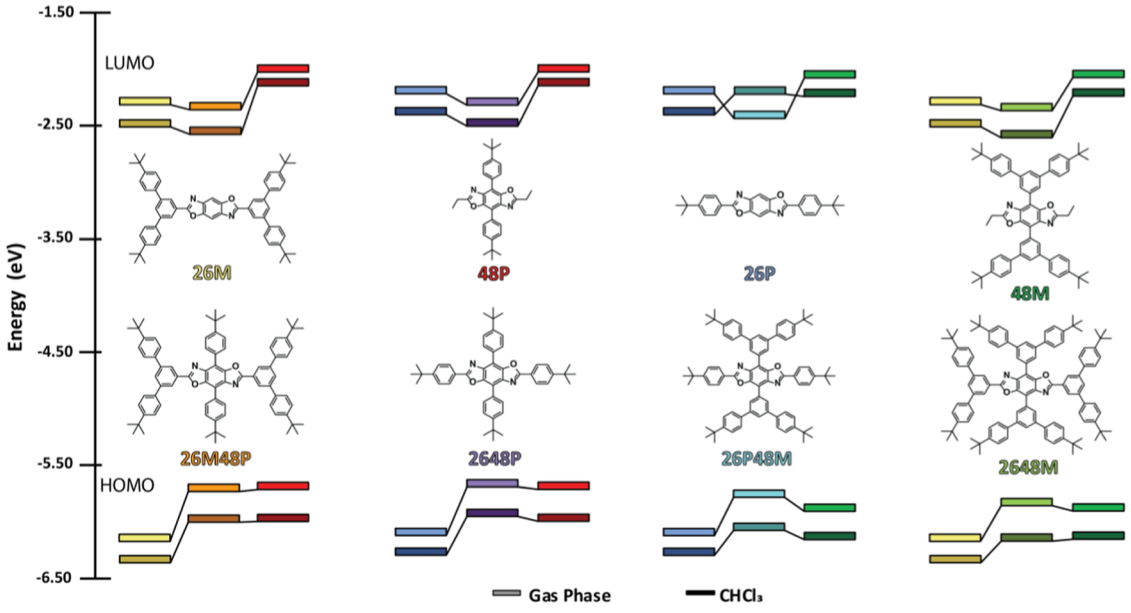

Figure 2. Band diagram based on the theoretical values. The light shade of a color indicates the gas-phase calculations, while the dark shade indicates calculations including CPCM.

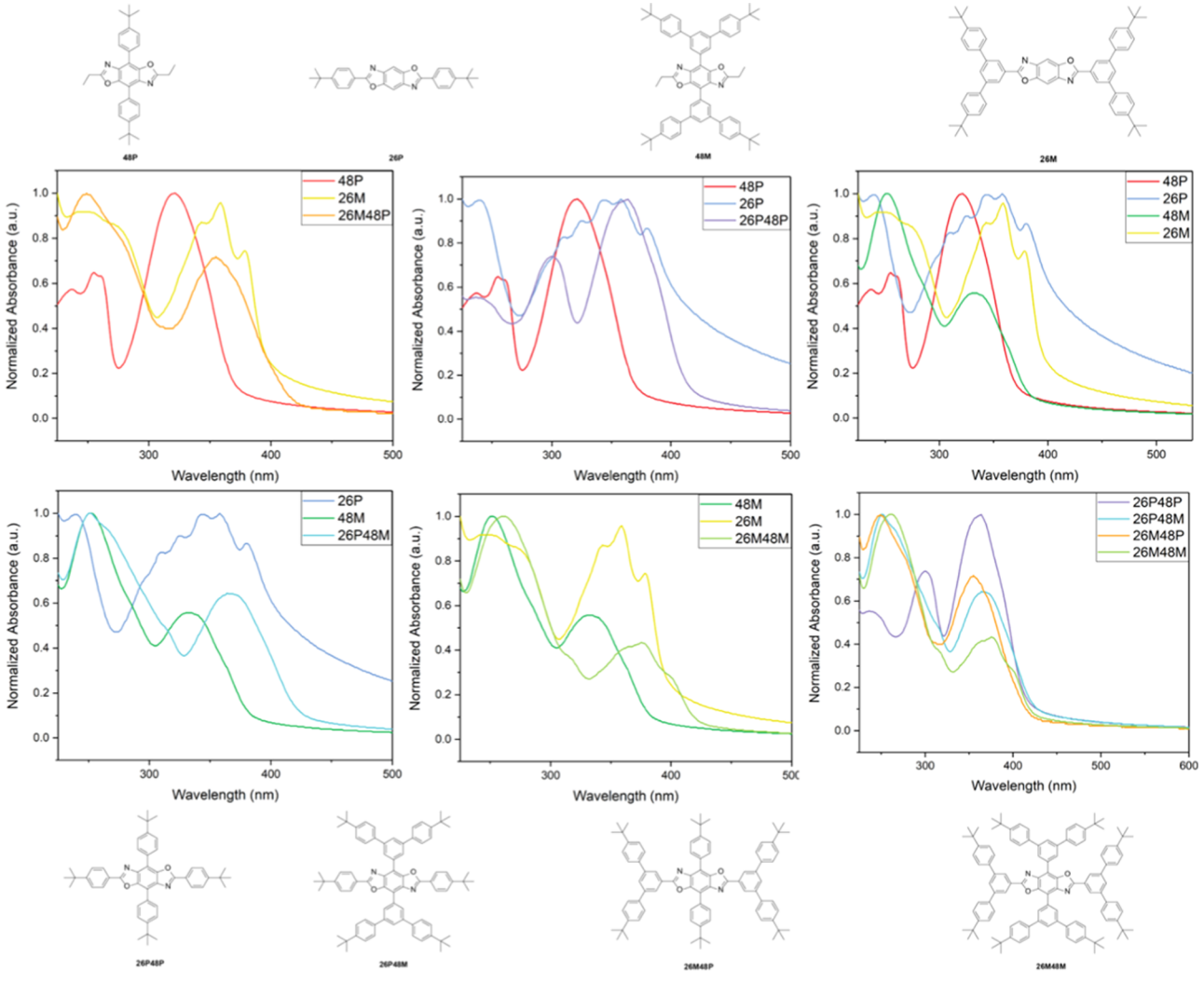

Figure 3. UV−vis spectra of the BBO small molecules as thin films.

https://dx.doi.org/10.1021/acsomega.0c01126
ACS Omega 2020, 5, 12374−12384

Table 2. Experimental (Solid-State) and Theoretical (Gas-Phase) Optical Properties of BBOs[a]

	solution state						DFT$_{gas}$	solid state			DFT$_{CHCl3}$
	E_g^{opt} (eV)										
BBO	exp't	DFT	Φ	$^{em}\lambda_{max}$ (nm)	ε (M/cm)	$^{abs}\lambda_{max}$ (nm)	λ (nm)	Φ[b]	$^{em}\lambda_{max}$ (nm)	$^{abs}\lambda_{max}$ (nm)	λ (nm)
26M	3.31	3.46	66	373, **393**, 415	1.9×10^5	332, **348**, 366	279, **355**	15	**403**, 542	244, 343, **359**, 379	280, **348**
26P	3.34	3.49	66	369, **389**, 411	2.2×10^5	330, **345**, 363	234, **344**	29	**449**	240, 309, 324, **359**, 381	265, **384**
48P	3.47	3.49	90	**364**, 382	1.6×10^5	**316**	265, **360**	27	**369**, 416, 446	237, 255, **321**	265, **355**
48M	3.48	3.53	68	**366**, 384	9.6×10^4	**317**	271, **349**	28	**396**	**251**, 332	277, **349**
26M48P	3.11	3.04	45	**410**, 431	2.2×10^5	**351**	**354**	23	**442**	**249**, 355	314, **367**
26P48P	3.14	3.09	44	406, **422**	2.1×10^5	291, **359**, 375	311, **355**	16	**431**	238, 299, **364**	309, **372**
26P48M	3.15	3.17	48	**398**, 421	2.1×10^5	**358**, 375	312, **355**	34	**451**	**251**, 364	310, **372**
26M48M	3.11	3.17	50	402, **424**	1.2×10^5	349, **364**, 381	**363**	22	**435**	**261**, 349, 364, 381	**369**

[a]Bold values are the peak of maximum absorbance/emission. [b]QYs include a slight overlap of the solvent excitation beam with emission.

has a calculated HOMO of −5.65 eV and LUMO of −2.28 eV, which correlates closely with the predicted HOMO for **48P** (−5.68 eV) and LUMO for **26M** (−2.27 eV) (Table 1). In the case of **26P48P**, the calculated HOMO of −5.66 eV and LUMO of −2.28 eV correspond well with the predicted HOMO for **48P** and LUMO for **26P** (−2.20 eV). Likewise, **26P48M** has a calculated HOMO of −5.76 eV and LUMO of −2.19 eV, which coincide with the predicted HOMO for **48M** (−5.87 eV) and LUMO for **26P**. Finally, **26M48M** has a calculated HOMO of −5.83 eV, which matches the predicted HOMO for **48M** (−5.87 eV). However, due to steric effects, the calculated LUMO for **26M48M** (−2.58 eV) differs from that for **26M** by 0.31 eV.

A comparison of the BBO siblings further elucidates the structure/property relationships in these systems. Cruciforms **26M48P** and **26P48P** both have phenyl substituents along the 4,8-axis resulting in degenerate HOMO levels. They also have similar LUMO values, leading to nearly identical E_g^{opt}. Thus, the steric effects of either substituent along the 2,6-axis are minimal as indicated by the small difference in the dihedral angle along either axis. Conversely, there is a significant steric effect along the 4,8-axis when the aryl groups are interchanged while holding the substituents along the 2,6-axis constant. In the case of **26P48M** and **26P48P**, there was a 13° decrease in the dihedral angle along with a 0.14 eV difference in the measured HOMO level, while the E_g^{opt} remained unchanged. Similarly, **26M48P** and **26M48M** have 9.7° and 0.42 eV differences in the dihedral angle and HOMOs, respectively, due to the increased sterics. However, the E_g^{opt} increased by ∼0.1 eV, thereby demonstrating that placing bulky groups along both axes has major steric implications, impacting both the HOMO levels and E_g^{opt}.

Optical Properties. The UV−visible spectra for the BBOs were experimentally measured in solution (Figure S20) and film states (Figure 3). Additionally, the predicted excited states, frontier molecular orbitals (FMOs), and simulated UV−vis spectra for each compound were generated using time-dependent DFT (TD-DFT) (see the Supporting Information (SI)). All relevant data are shown in Table 2, and experimental and theoretical overlays are provided in the SI. Herein, the evaluations of optical properties will be mainly focusing on the H → L transition as this is the primary transition of interest for future applications.

In solution, the optical transitions of each BBO are minimally affected by an increase in steric strain. Comparing **26P** and **26M**, these parents exhibit energetically similar transitions and retain identical peak morphology with only a 3 nm difference between peak maxima. A similar trend is observed comparing **48P** and **48M**. For both parent sets, the similarities in optical data are explained by the isoelectronic nature of the two compounds, thereby producing nearly identical H → L transition energies (E_g^{opt}). However, as the substituent that is placed in the 4,8-position is moved to the 2,6-position (such as in **48P** and **26P** and **48M** and **26M**), a red shift between absorbance spectra is observed, subsequently lowering the E_g^{opt}. This trend can be attributed to the increased planarization of the substituent in the 2,6-position as confirmed by DFT.

An evaluation of the four families provides valuable insight into what optical traits are inherited by the child from the parent. The optical transitions of the BBO child are energetically akin to their 2,6-parents, although the fine structure is diminished (Figure 3). Furthermore, the extended pi-system of the children results in a slight red shift in the absorption spectrum relative to that of their 2,6-parents. Initially, it appears that the 4,8-parents have very little influence on the low energy optical transitions. However, we believe the loss of fine structure observed in the cruciform spectra to be a result of the increased freedom of rotation the aryl groups exhibit when conjugated through the 4,8-axis. For all of the children, we see nearly identical optical spectra due to their isoelectronic properties.

As thin films, the optical properties of the BBO parents are primarily correlated to substituent location, with more prominent secondary influences due to the steric effects. For example, the axis of conjugation and its length for **48P** and **48M** are comparable, thereby giving rise to similar E_g^{opt} values and optical transitions. Conversely, for **26P** and **26M**, the E_g^{opt} values vary by approximately 0.2 eV due to the effective $\pi-\pi$ stacking between the **26P** molecules, which produces molecular transitions that are absent in **26M**. Thus, increasing sterics along the 2,6-axis does suppress particular optical transitions, whereas increasing sterics along the 4,8-axis does not. When the aryl group is held constant (**26P** vs **48P** and **26M** vs **48M**), conjugation through the 2,6-axis results in a red shift in the low energy transitions relative to the 4,8-analogue. The fine structure in both 2,6-parents is more visible, likely resulting from hydrogen bonding of the ortho-hydrogens on the aryl substituent to the oxazole heteroatoms on the BBO core, thereby locking the aryl substituent in place. For the HOMO and LUMO levels of each parent, the computational results show that the electron density is delocalized along the entire molecules, excluding the meta-conjugated phenyl rings

https://dx.doi.org/10.1021/acsomega.0c01126
ACS Omega 2020, 5, 12374−12384

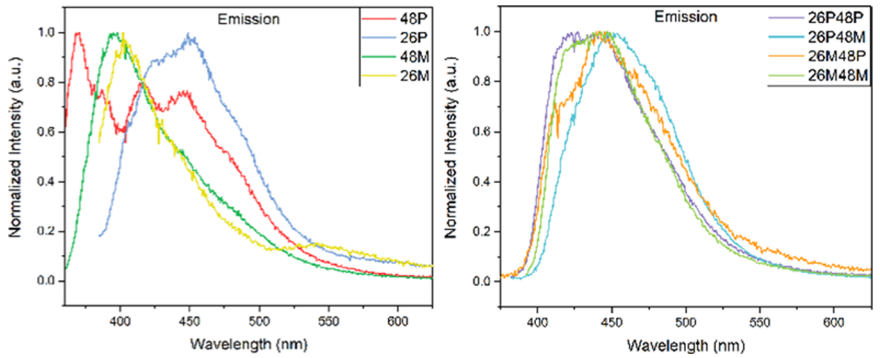

Figure 4. Photoluminescence of the BBO small molecules as thin films. Excitation was performed at the energetically lowest peak maxima from the UV−vis spectra.

in the **M** substituents, indicating strong locally excited-state character.

Next, we examined family groupings to evaluate which traits of the parents were inherited by the children, spectroscopically. For **26M48P**, the lower energy transitions observed for this cruciform (355 nm) appears to be inherited from the **26M** parent (359 nm) as **48P** had a transition at 321 nm. This effect produces an E_g^{opt} for **26M48P** (3.0 eV) that is nearly close to that of **26M** (3.1 eV). For **26P48P**, the lower energy transitions observed for this cruciform (364 nm) appears to be inherited from the **26P** parent (359 nm) as **48P** had a transition at 321 nm. This effect produces an E_g^{opt} of 2.9 eV for **26P48P** that is identical to that of **26P** (2.9 eV). For **26P48M**, the lower energy transitions observed for this cruciform (364 nm) appears to be inherited from the **26P** parent (359 nm) as **48M** had a transition at 332 nm. This effect produces an E_g^{opt} of 2.9 eV for **26P48M** that is the same for **26P** (2.9 eV). Finally, for **26M48M**, the lower energy transitions observed for this cruciform (364 nm) appears to be inherited from the **26M** parent (359 nm) as **48M** had a transition at 332 nm. This effect produces an E_g^{opt} of 2.9 eV for **26M48M** that is comparable to that of **26M** (3.1 eV). Therefore, the E_g^{opt} of the 2,6-parents can be used to predict the optical E_g^{opt} of the cross-conjugated child. For all children, the HOMO-level FMOs indicate that the electron density is found mainly on the aryl substituents conjugated through the 4,8-axis and on the BBO core alone. Upon excitation to the LUMO level, the electron density becomes delocalized throughout the entire molecule, excluding the meta-conjugated benzene rings.

The photoluminescence (PL) spectra for the BBOs were experimentally measured in solution (Figure S21) and film states (Figure 4). By keeping the conjugation axes the same (**48P** and **48M** and **26P** and **26M**), the emission profiles for both parent sets are practically the same (Figure S21). This observation is most likely due to the similar conjugation of molecules in each set. The peak maxima of the 4,8-parents were blue-shifted compared to that of the 2,6-analogues due to the increased E_g^{opt}. The children also exhibit very similar emissions based on their isoelectronic nature and the emissions are red-shifted compared to all of the parents due to the increased conjugation.

As thin films (Figure 4), all compounds exhibit bathochromic emission when compared to the corresponding solution spectrum. Interestingly, the emissive trends that are observed for the parents in solution are not observed in the film state. For the 4,8-parents, **48P** produces three major emission peaks (369, 416, and 446 nm) versus the single 396 nm peak emitted by **48M**. The multiband emission from **48P** is a result of the increased rotational freedom of the phenyl substituent, whereas **48M** is more sterically constrained. For the 2,6-parents, the emission peak for **26M** (403 nm) is blue-shifted relative to that for **26P** (449 nm) due to steric hindrance. Additionally, **26M** emitted at 547 nm, producing a hazy-blue/white luminescence. We believe this emission to be due to a slip-stack aggregate generated during film formation. For the children, the emission spectra are relatively unaffected by sterics as the peak morphology is quite similar and the absolute difference between each peak maximum is ≤20 nm.

CONCLUSIONS

In summary, using the heredity principle as a design motif, we modeled and synthesized a series of BBOs in which the optical and electronic properties of the linear parents were compared to those of the cross-conjugated children. All theoretical results were in good agreement with the experimental findings. For the parents, there was an inverse relationship between the HOMO energy and steric hindrance. The impact of sterics was the greatest when the bulky substituent was placed along the 2,6-axis. In all cases, the children inherited their HOMO energy from their 4,8-parents and the LUMO from the 2,6-parents. The optical E_g^{opt} values do not have a direct correlation to sterics in either the solution or solid state but are impacted by the effective conjugation length of the molecule. As thin films, each child exhibited electronic transitions energetically similar to their 2,6-parents, thereby producing similar E_g^{opt}. Each molecule was found to have unique emission maxima ≤451 nm, thereby making these ideal candidates for blue organic light-emitting diode (OLED) materials. Future works include evaluating the performance of these materials in OLEDs and investigating the impact of substituent type and position on device properties. Additional studies investigating the role of molecular heredity in the properties of organic semiconductors are also underway and will be reported in due course.

EXPERIMENTAL SECTION

Materials and Measurements. Br-DAHQ,[21] 2,5-diamino-3,6-dibromocyclohexa-2,5-diene-1,4-dione (Br-DAQ),[8] and 4,8-dibromo-2,6-diethylbenzobisoxazole[9] were synthesized according to literature procedures. Tetrahydrofuran (THF) was dried using an Innovative Technologies solvent purification system. All other chemical reagents were purchased from commercial sources and used without further purification unless otherwise noted. Nuclear magnetic resonance (NMR)

https://dx.doi.org/10.1021/acsomega.0c01126
ACS Omega 2020, 5, 12374−12384

experiments were carried out in $CDCl_3$ at 500 MHz (^1H) and 125 MHZ (^{13}C). In all spectra, chemical shifts are given in δ relative to the residual protonated solvent peak, $CHCl_3$ (7.26 ppm, ^1H; 77.16 ppm, ^{13}C). Coupling constants are reported in hertz (Hz). High-resolution mass spectra were recorded on a double-focusing magnetic sector mass spectrometer using ESI. All UV−vis and fluorescence spectroscopy were obtained using quartz cuvettes with a 10 mm path length in $CHCl_3$ (1×10^{-6} M) for the solution state or as spin-cast thin films on a quartz slide (5 mg/mL solution in $CHCl_3$ spun at 1500 RPM). UV−vis spectra were collected on a Shimadzu UV-1800 UV spectrophotometer. Photoluminescence spectra were obtained on a Varian Cary Eclipse spectrophotometer. Absolute solution fluorescence quantum yields were obtained using a HORIBA Nanolog FL3-2iHR spectrophotometer equipped with a Quanta-phi integrating sphere. Ultraviolet photoelectron spectroscopy (UPS) was used to acquire the ionization potentials and approximate the HOMO values for each material. All substrates (positively doped silicon; 10 × 10 mm^2) had 40 nm of silver deposited via thermal evaporation. Samples were prepared by dissolution in $CHCl_3$ at a concentration of 5 mg/mL and stirred for a minimum of 4 h. Each solution was filtered to remove potential aggregates and sequentially spin-coated under a nitrogen atmosphere at 4000 RPM. Spectra were then acquired under ultrahigh vacuum at random positions on the formed film. Thermal gravimetric analysis (TGA) was performed using a TA Instruments TGA Q50 machine, at a scan rate of 10 °C/min under a nitrogen atmosphere. Differential scanning calorimetry was performed using a TA Instruments Q series calorimeter.

Synthesis of Precursors. *4-(tert-Butyl)-benzaldehyde (**1**).* This precursor was prepared similar to literature procedures.[22] To an oven-dried round bottom flask (RBF) purged with N_2 were added 20 mL of anhydrous THF and 1.73 mL (10 mmol) of 4-(*tert*-butyl)bromobenzene. The solution was brought to −78 °C followed by the dropwise addition of *n*-butyllithium (2.5 M in hexanes, 4.8 mL). After an hour of stirring, 0.93 mL of anhydrous DMF was added and the solution was brought to room temperature for overnight stirring. Diethyl ether and distilled water were poured into the flask and the organic layer was separated. The organic layer was subjected to two aqueous washes and drying over $MgSO_4$. The solvent was removed and was used without purification. ^1H NMR (500 MHz, $CDCl_3$) δ 9.95 (s, 1H), 7.79 (d, J = 8.6 Hz, 2H), 7.52 (d, J = 8.4 Hz, 2H) ^{13}C (125 MHz, $CDCl_3$) δ 191.9, 158.3, 134.1, 129.6, 125.9, 35.3, 31.0.

*(4-(tert-Butyl)phenyl)boronic Acid (**2**).* This precursor was prepared similar to literature procedures.[23] To an oven-dried RBF purged with N_2 was added 0.80 g (33 mmol) of dried magnesium turnings. The flask was purged three times with N_2 before the addition of 30 mL of anhydrous THF. Following this was added 4-(*tert*-butyl)bromobenzene (5.2 mL, 30 mmol), and the solution was heated to 45 °C for 1 h. The solution slowly cooled to room temperature and had an additional 30 mL of anhydrous THF added. The contents were bought to −78 °C followed by the dropwise addition of trimethylborate (3.9 mL, 35 mmol). The solution was allowed to naturally come to room temperature with overnight stirring. The white paste formed was acidified with 2 M HCl, dissolving the solid. The solution stirred for an additional hour before extracting in Et_2O. The organic layer was washed twice with water, dried over Na_2SO_4, and concentrated onto silica for separation using column chromatography (hex/EtAc gradient). The product was isolated as a white solid (4.00 g, 75%). ^1H NMR (500 MHz, $CDCl_3$) δ 8.27 (d, J = 7.9 Hz, 2H), 7.56 (d, J = 8.0 Hz, 2H), 1.40 (s, 9H) ^{13}C (125 MHz, $CDCl_3$) δ 156.0, 135.6, 124.9, 35.1, 31.2.

*3,5-Dibromobenzaldehyde (**3**).* To an oven-dried RBF purged with N_2 were added syn-tribromobenzene (1.89 g, 6 mmol) and anhydrous Et_2O (30 mL). The solution was brought to −78 °C for five min before the dropwise addition of *n*-butyllithium (2.5 M in hexanes, 2.5 mL) and stirred at this temperature for 3 h before the addition of anhydrous DMF (0.5 mL, 6.5 mmol). Afterward, the solution was allowed to slowly come to room temperature by overnight stirring before distilled H_2O was added to the flask. The organic layer was taken up in Et_2O, washed twice with distilled water, dried over $MgSO_4$, and concentrated onto silica gel. Column chromatography (hex/EtAc gradient) was used to isolate the products as a white solid (1.11 g, 70%). ^1H NMR (500 MHz, $CDCl_3$) δ 9.90 (s, 1H), 7.94 (d, J = 1.8 Hz, 2H), 7.92 (t, J = 1.7 Hz, 1H). ^{13}C (125 MHz, $CDCl_3$) δ 189.0, 139.6, 138.9, 131.2, 123.9.

*4,4″-Di-tert-butyl-[1,1′:3′,1″-terphenyl]-5′-carbaldehyde (**4**).* This precursor was prepared similar to literature procedures.[24] To a N_2-purged flask were added **1** (1.30 g, 7.3 mmol), **2** (0.77 g, 2.9 mmol), and toluene (30 mL). The solution was degassed for 30 min before the addition of one drop of Aliquot 336, tetrakis(triphenylphosphine) palladium(0) (0.16 g, 0.14 mmol), and degassed 2 M K_2CO_3 (4.4 mL) in that order. The solution was brought to reflux for overnight stirring and cooled to room temperature. Ethyl acetate was poured into the reaction mixture, and the organic layer was washed twice with H_2O, dried over Na_2SO_4, and concentrated onto silica. Column chromatography (hex/EtAc) was used to separate the product as a white solid (1.00 g, 93%). ^1H NMR (500 MHz, $CDCl_3$) δ 10.14 (s, 1H), 8.07 (t, J = 1.8 Hz, 1H), 8.05 (d, J = 1.7 Hz, 2H), 7.63 (d, J = 8.6 Hz, 4H), 7.53, (d, J = 8.5 Hz, 4H), 1.39 (s, 18H). ^{13}C (125 MHz, $CDCl_3$) δ 192.4, 151.2, 142.5, 137.4, 136.9, 131.6, 126.9, 126.8, 126.0, 34.7, 31.4.

*(3,5-Dibromophenyl)trimethylsilane (**5**).* This precursor was prepared similar to literature procedures.[25] To an oven-dried RBF purged with N_2 were added syn-tribromobenzene (6.30 g, 20 mmol) and anhydrous Et_2O (50 mL). The solution was brought to −78 °C for 10 min before the dropwise addition of *n*-butyllithium (2.5 M in hexanes, 8.2 mL). The solution was stirred at this temperature for 3 h before the addition of trimethylchlorosilane (2.8 mL, 22 mmol). The solution was allowed to warm to room temperature for overnight stirring. Excess Et_2O was added to the flask along with distilled water. The solution stirred for 10 min before separating the organic layer, which was washed once more with water, dried over $MgSO_4$, and concentrated onto silica. Column chromatography (silica/hexanes) was used to isolate the product as an orange oil (5.61 g, 91%). ^1H NMR (500 MHz, $CDCl_3$) δ 7.65 (t, J = 1.8 Hz, 1H), 7.53 (d, J = 1.8 Hz, 2H), 0.29 (s, 9H). ^{13}C (125 MHz, $CDCl_3$) δ 146.0, 134.5, 134.2, 123.2, −1.33.

*(4,4″-Di-tert-butyl-[1,1′:3′,1″-terphenyl]-5′-yl)-trimethylsilane (**6**).* This precursor was prepared similar to the literature procedures.[24] To a N_2-purged flask were added **1** (4.45 g, 25.0 mmol), **3** (3.06 g, 9.9 mmol), and toluene (30 mL). The solution was degassed for 30 min before the addition of one drop of Aliquot 336, tetrakis(triphenylphosphine) palladium(0) (0.60 g, 0.5 mmol), and degassed 2 M K_2CO_3 (14 mL) in that order. The solution was brought to reflux for

https://dx.doi.org/10.1021/acsomega.0c01126
ACS Omega 2020, 5, 12374−12384

overnight stirring and cooled to room temperature. Ethyl acetate was poured into the reaction mixture, and the organic layer was washed twice with H_2O, dried over Na_2SO_4, and concentrated onto silica. Column chromatography (hexanes) was used to separate a mixture of mono- and di-coupled products. The oil was brought to 0 °C and sonicated to induced solidification. After approx. 24 h, the solid/oil mixture was sonicated in minimal methanol and filtered to isolate the product as a white solid (2.32 g, 56%). ^{1}H NMR (500 MHz, $CDCl_3$) δ 7.77 (t, J = 1.8 Hz, 1H), 7.68 (d, J = 1.8 Hz, 2H), 7.59 (d, J = 8.4 Hz, 4H), 7.50 (d, J = 8.5 Hz, 4H), 1.39 (s, 18H), 0.34 (s, 9H).

*(4,4″-Di-tert-butyl-[1,1′:3′,1″-terphenyl]-5′-yl)boronic Acid (**7**).* This precursor was prepared similar to the literature procedures.[26] To an oven-dried RBF purged with N_2 were added **5** (1.74 g, 4.2 mmol) and 10 mL of DCM. The solution was brought to −78 °C, and 0.66 mL (6.8 mmol) of boron tribromide was added. The solution stirred for 1 h before being brought to room temperature and finally brought to reflux for 18 h. Afterward, the solution was cooled back to −78 °C for the addition of 5 mL (25 mmol) of a 5 M KOH solution, which was added through the top of the condenser. The solution was brought back to room temperature by stirring for an hour, diluted with Et_2O, and then acidified using 2 M HCl. The organic layer was separated, washed twice with distilled water, dried over Na_2SO_4, and concentrated onto silica. Column chromatography (hex/EtAc gradient) was used to separate the product as a slightly pink solid (1.26 g, 77%).^{1}H NMR (500 MHz, $CDCl_3$) δ 8.46 (d, J = 1.6 Hz, 2H), 8.05 (t, J = 1.6 Hz, 1H), 7.72, (d, J = 8.3 Hz, 4H), 7.57 (d, J = 8.3 Hz, 4H), 1.42 (s, 18H). ^{13}C (125 MHz, $CDCl_3$) δ 150.5, 141.2, 138.3, 133.1, 130.3, 127.1, 125.9, 34.6, 31.4.

General Procedure for the Formation of 26P48Br and 26M48Br. The starting benzaldehyde (2.5 mmol equiv), Br-DAQ (1 mmol equiv), and 30 mol % $CuSO_4$ were added to a pressure flask (aerobic atmosphere) along with 10 mL of reagent alcohol and heated to 155 °C for 2.5 h. Afterward, the suspension was cooled to room temperature (RT) and transferred to a different flask, fitted with septa and a needle for ventilation. H_2O_2 (30%; 10 mmol equiv) was added dropwise to the solution, and the solution was then brought to 90 °C for 1 h. The solid was then filtered, stirred in hot hexanes, filtered again, and dried. **26P48Br** was formed in 53% yield, and **26M48Br** was formed in 85% yield. We were unable to obtain decent ^{1}H NMR spectra for the precursors.

General Procedure for the Formation of 26P and 26M. This precursor was prepared similar to the literature procedures.[27] The starting benzaldehyde (3 mmol), DAQ (1 mmol), and four drops of piperdine were added to a round bottom flask (aerobic atmosphere) with 10 mL of reagent alcohol and heated at 85 °C for 24 h. Afterward, the suspension was cooled to RT and transferred to a different flask and fitted with septa and a needle for ventilation. H_2O_2 (30%; 10 mmol equiv) was added dropwise to the solution, and the solution was then brought back to 90 °C for 12 h. The solid was then filtered and recrystallized in specific solvents. The solvents used, corresponding yields, and ^{1}H NMR spectra are shown below for the respective intermediates.

*2,6-Bis(4,4″-di-tert-butyl-[1,1′:3′,1″-terphenyl]-5′-yl)-benzo[1,2-d:4,5-d′]bis(oxazole) (**26M**).* $CHCl_3$ used for recrystallization (mp > 230 °C, 13%). ^{1}H NMR (500 MHz, $CDCl_3$) δ 8.49 (d, J = 1.5 Hz, 4H), 8.00 (t, J = 1.7 Hz, 2H), 7.99 (s, 2H), 7.71 (d, J = 8.3 Hz, 8H), 7.54 (d, J = 8.2 Hz, 8H), 1.40 (s, 36H). HRMS (ESI) m/z: $[M + H]^+$ calcd for $C_{60}H_{61}N_2O_2$: 841.4733; found: 841.4745.

*2,6-Bis(4-(tert-butyl)phenyl)benzo[1,2-d:4,5-d′]bis-(oxazole) (**26P**).* THF used for recrystallization (mp > 230 °C, 10%). ^{1}H NMR (500 MHz, $CDCl_3$) δ 8.21 (d, J = 8.4 Hz, 4H), 7.90 (s, 2H), 7.57 (d, J = 8.4 Hz, 4H), 1.39 (s, 18H). ^{13}C (125 MHz, $CDCl_3$) δ 164.4, 155.3, 148.4, 140.3, 127.4, 126.0, 124.2, 100.7, 35.1, 31.1. HRMS (ESI) m/z: $[M + H]^+$ calcd for $C_{26}H_{29}N_2O_2$: 425.2229; found: 425.2249

General Procedure for the Final Suzuki−Miyaura Coupling. This precursor was prepared similar to the literature procedures.[28] The general procedure is as follows: 0.2 mmol of either 4,8-dibromo-2,6-diethylbenzobisoxazole, 26P48Br, or 26M48Br was added to a 75 mL pressure flask along with 5% mol equiv PEPPSI-*i*Pr, 0.5 mmol of **6** or **11**, and 1.3 mmol of cesium fluoride, to the same flask, were added. These contents were dissolved in 10 mL of THF and degassed for 15 min. Afterward, the flask was sealed and heated to 130 °C for 12 h. After cooling to room temperature, the crude solution was diluted with DCM and concentrated onto silica gel for solid-loaded column chromatography using hexanes/$CHCl_3$ as the eluent to produce pure products. We were unable to obtained ^{13}C spectra for all cruciforms due to their poor solubility.

*4,8-Bis(4,4″-di-tert-butyl-[1,1′:3′,1″-terphenyl]-5′-yl)-2,6-diethylbenzo[1,2-d:4,5-d′]bis(oxazole) (**48M**).* (Mp > 230 °C, 61%). ^{1}H NMR (500 MHz, $CDCl_3$) δ 8.42 (d, J = 1.7 Hz, 4H), 7.88, (t, J = 1.7 Hz, 2H), 7.72, (d, J = 8.2 Hz, 8H), 7.54 (d, J = 8.3 Hz, 8H), 3.07 (q, J = 7.6 Hz, 4H), 1.54 (t, J = 7.6 Hz, 6H), 1.40 (s, 36H) HRMS (ESI) m/z: $[M + H]^+$ calcd for $C_{64}H_{69}N_2O_2$: 897.5359; found: 897.5362.

*4,8-Bis(4-(tert-butyl)phenyl)-2,6-diethylbenzo[1,2-d:4,5-d′]bis(oxazole) (**48P**).* (Mp > 230 °C, 82%). ^{1}H NMR (500 MHz, $CDCl_3$) δ 8.17 (d, J = 8.4 Hz, 4H), 7.60 (d, J = 8.4 Hz, 4H), 3.04 (q, J = 7.6 Hz, 4H), 1.49 (t, J = 7.6 Hz, 6H). ^{13}C (125 MHz, $CDCl_3$) δ 168.6, 150.9, 146.0, 136.9, 129.7, 129.6, 125.6, 113.6, 34.7, 31.3, 22.6, 11.4. HRMS (ESI) m/z: $[M + H]^+$ calcd for $C_{32}H_{37}N_2O_2$: 481.2855; found: 481.2876.

*2,4,6,8-Tetrakis(4,4″-di-tert-butyl-[1,1′:3′,1″-terphenyl]-5′-yl)benzo[1,2-d:4,5-d′]bis(oxazole) (**26M48M**).* (Mp > 230 °C, 13%). ^{1}H NMR (500 MHz, $CDCl_3$) δ 8.47 (d, J = 1.5 Hz, 4H), 8.68 (d, J = 1.6 Hz, 4H), 8.05 (t, J = 1.5 Hz, 2H), 7.97 (t, J = 1.5 Hz, 2H), 7.86 (d, J = 8.4 Hz, 8H), 7.77 (d, J = 8.3 Hz, 8H), 7.55 (d, J = 8.7 Hz, 8H), 7.53 (d, J = 8.6 Hz, 8H), 1.40 (s, 72H). HRMS (ESI) m/z: $[M + H]^+$ calcd for $C_{112}H_{117}N_2O_2$: 1521.9115; found: 1522.215

*4,8-Bis(4-(tert-butyl)phenyl)-2,6-bis(4,4″-di-tert-butyl-[1,1′:3′,1″-terphenyl]-5′-yl)benzo[1,2-d:4,5-d′]bis(oxazole) (**26M48P**).* (Mp > 230 °C, 37%). ^{1}H NMR (500 MHz, $CDCl_3$) δ 8.49 (m, 4H), 8.40 (d, J = 8.2 Hz, 4H), 7.93 (m, 2H), 7.70 (m, 12H), 7.55 (d, J = 7.9 Hz, 8H), 1.47 (s, 18H), 1.41 (s, 36H). HRMS (ESI) m/z: $[M + H]^+$calcd for $C_{80}H_{85}N_2O_2$: 1105.6611; molecular ion not found.

*2,6-Bis(4-(tert-butyl)phenyl)-4,8-bis(4,4″-di-tert-butyl-[1,1′:3′,1″-terphenyl]-5′-yl)benzo[1,2-d:4,5-d′]bis(oxazole) (**26P48M**).* (Mp > 230 °C, 20%). ^{1}H NMR (500 MHz, $CDCl_3$) δ 8.61 (d, J = 1.5 Hz, 4H), 8.29 (d, J = 8.5 Hz, 4H), 7.96 (t, J = 1.5 Hz, 2H), 7.80 (d, J = 8.3 Hz, 8H), 7.59−7.55 (m, 12H), 1.42 (s, 36H), 1.40 (s, 18H). HRMS (ESI) m/z: $[M + H]^+$ calcd for $C_{80}H_{85}N_2O_2$: 1105.6611; found: 1105.6664

*2,4,6,8-Tetrakis(4-(tert-butyl)phenyl)benzo[1,2-d:4,5-d′]-bis(oxazole) (**26P48P**).* (Mp > 230 °C, 17%). ^{1}H NMR (500 MHz, $CDCl_3$) δ 8.41, (d, J = 8.4 Hz, 4H), 8.28 (d, J = 8.3 Hz,

https://dx.doi.org/10.1021/acsomega.0c01126
ACS Omega 2020, 5, 12374−12384

4H), 7.68 (d, J = 8.5 Hz, 4H), 7.56 (d, J = 8.3 Hz, 4H), 1.46 (s, 18H), 1.39 (s, 18H). ^{13}C (125 MHz, $CDCl_3$) δ 163.7, 155.0, 151.1, 146.3, 138.3, 129.9, 129.8, 127.6, 125.8, 125.6, 124.5, 113.8, 35.1. 34.8, 31.4, 31.2. HRMS (ESI) m/z: $[M + H]^+$ calcd for $C_{48}H_{532}N_2O_2$: 689.4107; found: 689.4094.

Computational Details. All computations were performed using Gaussian09 by the Comet supercomputer cluster provided by the San Diego Supercomputing Center through the Extreme Science and Engineering Discovery Environment (XSEDE). They were then analyzed through GaussView 6 GUI interface program package. All benchmarking efforts and results, which led to the chosen functional and basis set, are outlined in previous work.[10] Electronic ground-state geometries were optimized using density functional theory (DFT), employing the mPW3PBE functional and the SV basis set verified through a frequency calculation both with and without chloroform inclusion through the conductor polarizable calculation model (CPCM). Excited states for both phases were generated through time-dependent density functional theory (TD-DFT) applied to the optimized ground state for each oligomer. The HOMOs, LUMOs, band gaps, first 15 excited states, FMOs, and UV−vis simulations were generated from these computations.

■ ASSOCIATED CONTENT

Supporting Information

The Supporting Information is available free of charge at https://pubs.acs.org/doi/10.1021/acsomega.0c01126.

^{1}H and ^{13}C NMR spectra, TGA data, DSC data, DFT Cartesian coordinates, solution-state UV−vis and photoluminescence spectra, comparison of experimental and DFT UV−vis results, geometric images, and frontier molecular orbitals (PDF)

■ AUTHOR INFORMATION

Corresponding Author

Malika Jeffries-EL − *Department of Chemistry and Division of Materials Science and Engineering, Boston University, Boston, Massachusetts 02215, United States;* orcid.org/0000-0002-9134-4938; Phone: (617) 353-2500; Email: malikaj@bu.edu

Authors

David L. Wheeler − *Department of Chemistry, Boston University, Boston, Massachusetts 02215, United States*

Alex V. Diodati − *Department of Chemistry and Biochemistry, University of North Georgia, Dahlonega, Georgia 30041, United States; Department of Chemistry, University of Florida, Gainesville, Florida 32603, United States*

Aimée L. Tomlinson − *Department of Chemistry and Biochemistry, University of North Georgia, Dahlonega, Georgia 30041, United States*

Complete contact information is available at: https://pubs.acs.org/10.1021/acsomega.0c01126

Notes

The authors declare no competing financial interest.

■ ACKNOWLEDGMENTS

We thank the National Science Foundation (CHE-1808402 and CHE-1808414) as well supercomputer allocation from XSEDE (DMR-160146) for providing financial support to this work. We also thank Prof. Mark Grinstaff (BU) for TGA and DSC access, Dr. Paul Ralifo and Dr. Norman Lee of the CIC for NMR and HRMS access and measurements, respectively, Dr. Allison (BU) Dennis for integrating sphere access for quantum yield measurements, and Dr. Volodimyr Duzhko, the Director of the Laboratory for Electronic Materials and Devices at the University of Massachusetts, Amherst, for guidance and insight into UPS measurements.

■ REFERENCES

(1) Borges-González, J.; Kousseff, C. J.; Nielsen, C. B. Organic semiconductors for biological sensing. *J. Mater. Chem. C* **2019**, *7*, 1111−1130.

(2) Shahnawaz, S.; Swayamprabha, S.; Nagar, M. R.; Yadav, R. A. K.; Gull, S.; Dubey, D. K.; Jou, J.-H. Hole-transporting materials for organic light-emitting diodes: an overview. *J. Mater. Chem. C* **2019**, *7*, 7144−7158.

(3) Yang, X.; Xu, X.; Zhou, G. Recent advances of the emitters for high performance deep-blue organic light-emitting diodes. *J. Mater. Chem. C* **2015**, *3*, 913−944.

(4) He, X.; Yin, L.; Li, Y. Design of organic small molecules for photovoltaic application with high open-circuit voltage (Voc). *J. Mater. Chem. C* **2019**, *7*, 2487−2521.

(5) Kanibolotsky, A. L.; Laurand, N.; Dawson, M. D.; Turnbull, G. A.; Samuel, I. D. W.; Skabara, P. J. Design of Linear and Star-Shaped Macromolecular Organic Semiconductors for Photonic Applications. *Acc. Chem. Res.* **2019**, *52*, 1665−1674.

(6) Xie, Z.; Chen, C.; Xu, S.; Li, J.; Zhang, Y.; Liu, S.; Xu, J.; Chi, Z. White-Light Emission Strategy of a Single Organic Compound with Aggregation-Induced Emission and Delayed Fluorescence Properties. *Angew. Chem., Int. Ed.* **2015**, *54*, 7181−7184.

(7) Xu, B.; Mu, Y.; Mao, Z.; Xie, Z.; Wu, H.; Zhang, Y.; Jin, C.; Chi, Z.; Liu, S.; Xu, J.; Wu, Y.-C.; Lu, P.-Y.; Lien, A.; Bryce, M. R. Achieving remarkable mechanochromism and white-light emission with thermally activated delayed fluorescence through the molecular heredity principle. *Chem. Sci.* **2016**, *7*, 2201−2206.

(8) Tlach, B. C.; Tomlinson, A. L.; Bhuwalka, A.; Jeffries-El, M. Tuning the Optical and Electronic Properties of 4,8-Disubstituted Benzobisoxazoles via Alkyne Substitution. *J. Org. Chem.* **2011**, *76*, 8670−8681.

(9) Tlach, B. C.; Tomlinson, A. L.; Ryno, A. G.; Knoble, D. D.; Drochner, D. L.; Krager, K. J.; Jeffries-El, M. Influence of Conjugation Axis on the Optical and Electronic Properties of Aryl-Substituted Benzobisoxazoles. *J. Org. Chem.* **2013**, *78*, 6570−6581.

(10) Chavez, R., III; Diodati, L.; Wheeler, D. L.; Shaw, J.; Tomlinson, A. L.; Jeffries-El, M. Evaluating the Impact of Fluorination on the Electro-optical Properties of Cross-Conjugated Benzobisoxazoles. *J. Phys. Chem. A* **2019**, *123*, 1343−1352.

(11) Chavez, R., III; Cai, M.; Tlach, B.; Wheeler, D. L.; Kaudal, R.; Tsyrenova, A.; Tomlinson, A. L.; Shinar, R.; Shinar, J.; Jeffries-El, M. Benzobisoxazole cruciforms: a tunable, cross-conjugated platform for the generation of deep blue OLED materials. *J. Mater. Chem. C* **2016**, *4*, 3765−3773.

(12) Yin, X.; Zhang, T.; Peng, Q.; Zhou, T.; Zeng, W.; Zhu, Z.; Xie, G.; Li, F.; Ma, D.; yang, c. Benzobisoxazole-based electron transporting materials with high Tg and ambipolar property: high efficiency deep-red phosphorescent OLEDs. *J. Mater. Chem. C* **2015**, *3*, 7589−7596.

(13) Intemann, J. J.; Hellerich, E. S.; Ewan, M. D.; Tlach, B. C.; Speetzen, E. D.; Shinar, R.; Shinar, J.; Jeffries-El, M. Investigating the impact of conjugation pathway on the physical and electronic properties of benzobisoxazole-containing polymers. *J. Mater. Chem. C* **2017**, *5*, 12839−12847.

(14) Lim, J.; Albright, T. A.; Martin, B. R.; Miljanić, O. Š. Benzobisoxazole Cruciforms: Heterocyclic Fluorophores with Spatially Separated Frontier Molecular Orbitals. *J. Org. Chem.* **2011**, *76*, 10207−10219.

(15) Reinhardt, B. A.; Unroe, M. R.; Evers, R. C.; et al. Third-Order Optical Nonlinearities of Model Compounds Containing Benzobisthiazole, Benzobisoxazole and Benzbisimidazole Units. *Chem. Mater.* **1991**, *3*, 864−71.
(16) Mike, J. F.; Intemann, J. J.; Cai, M.; Xiao, T.; Shinar, R.; Shinar, J.; Jeffries-EL, M. Efficient synthesis of benzobisazole terpolymers containing thiophene and fluorene. *Polymer Chemistry* **2011**, *2*, 2299−2305.
(17) Jois, Y. H. R.; Gibson, H. W. Difunctional Heterocycles: A Convenient One Pot Synthesis of Novel Bis(benzoxazoles) from Bis(o-aminophenol)s. *J. Heterocycl. Chem.* **1992**, *29*, 1365−1368.
(18) Salaneck, W. R. Classical ultraviolet photoelectron spectroscopy of polymers. *J. Electron Spectrosc. Relat. Phenom.* **2009**, *174*, 3−9.
(19) Miyamae, T.; Yoshimura, D.; Ishii, H.; Ouchi, Y.; Miyazaki, T.; Koike, T.; Yamamoto, T.; Muramatsu, Y.; Etori, H.; Maruyama, T.; Seki, K. Ultraviolet photoelectron spectroscopy of n-type conducting polymers. *Synth. Met.* **1997**, *84*, 939−940.
(20) Lois, S.; Florès, J.-C.; Lère-Porte, J.-P.; Serein-Spirau, F.; Moreau, J. J. E.; Miqueu, K.; Sotiropoulos, J.-M.; Baylère, P.; Tillard, M.; Belin, C. How to Build Fully π-Conjugated Architectures with Thienylene and Phenylene Fragments. *Eur. J. Org. Chem.* **2007**, *2007*, 4019−4031.
(21) Hegedus, L. S.; Odle, R. R.; Winton, P. M.; Weider, P. R. Synthesis of 2,5-disubstituted 3,6-diamino-1,4-benzoquinones. *J. Org. Chem.* **1982**, *47*, 2607−2613.
(22) Kinena, L. et al. Substituted Aminoalkylazoles As Malarial Aspartic Protease Inhibitors. WO Patent WO2017069601A12013.
(23) Watanabe, M.; Tsuchiya, K.; Shinnai, T.; Kijima, M. Liquid Crystalline Polythiophene Bearing Phenylnaphthalene Side-Chain. *Macromolecules* **2012**, *45*, 1825−1832.
(24) Sevov, C. S.; Hartwig, J. F. Iridium-Catalyzed Oxidative Olefination of Furans with Unactivated Alkenes. *J. Am. Chem. Soc.* **2014**, *136*, 10625−10631.
(25) Bonn, A. G.; Yushchenko, O.; Vauthey, E.; Wenger, O. S. Photoinduced Electron Transfer in an Anthraquinone−[Ru(bpy)3]-2+−Oligotriarylamine−[Ru(bpy)3]2+−Anthraquinone Pentad. *Inorg. Chem.* **2016**, *55*, 2894−2899.
(26) Miller, T. M.; Neenan, T. X.; Zayas, R.; Bair, H. E. Synthesis and characterization of a series of monodisperse, 1,3,5-phenylene-based hydrocarbon dendrimers including C276H186 and their fluorinated analogs. *J. Am. Chem. Soc.* **1992**, *114*, 1018−1025.
(27) Osman, A.-M. Benzdioxazoles. *J. Am. Chem. Soc.* **1957**, *79*, 966−968.
(28) Sharma, A. K.; Gowdahalli, K.; Krzeminski, J.; Amin, S. Microwave-Assisted Suzuki Cross-Coupling Reaction, a Key Step in the Synthesis of Polycyclic Aromatic Hydrocarbons and Their Metabolites. *J. Org. Chem* **2007**, *72*, 8987−8989.

https://dx.doi.org/10.1021/acsomega.0c01126
ACS Omega 2020, 5, 12374−12384